Exp Brain Res (1993) 94:183–192

Experimental Brain Research

Interpretation of high-resolution current source density profiles: a simulation of sublaminar contributions to the visual evoked potential

Craig E. Tenke[1], **Charles E. Schroeder**[2,3], **Joseph C. Arezzo**[2,3], **Herbert G. Vaughan, Jr.**[2,3,4]

[1] Department of Biopsychology, NYS Psychiatric Institute, New York, New York, USA
[2] Department of Neuroscience, Albert Einstein College of Medicine, Bronx, New York, USA
[3] Department of Neurology, Albert Einstein College of Medicine, Bronx, New York, USA
[4] Department of Pediatrics, Albert Einstein College of Medicine, Bronx, New York, USA

Received: 9 September 1992 / Accepted: 11 November 1992

Abstract. Current source density (CSD) analysis provides an index of the location, direction, and density of transmembrane currents that arise with synchronous activation of neural tissue and that generate an evoked potential profile in the extracellular medium. In neocortex and other laminated structures, a simplified, one-dimensional CSD analysis can be computed by differentiation of voltages sampled at discrete points in a linear array. One-dimensional CSD analysis is a practical and accurate method for defining both regional activity patterns and neural generators of surface-recorded evoked and event-related potentials. In computing the CSD, common practices of differentiating across spatial grids of 200 μm or more and use of spatial smoothing routines help to reduce noise, but severely limit the spatial resolution available to the analysis. High-resolution CSD procedures (i.e., 3 point differentiation using a spatial grid of 100 μm or less) are more suited to identification of processes within individual cortical laminae or sublaminae, but can magnify the contributions of computational artifacts. Despite the inclusion of independent indices of cellular activity (e.g., multiunit activity), both high- and low-resolution analyses may indicate current source and sink configurations for which there is more than one plausible physiological interpretation. In the present study we examined the resolving capacity and pitfalls of common CSD procedures using simulated ensembles of current dipoles. These were positioned and oriented to model the depolarization of lamina 4C stellate cells and thalamocortical afferents in macaque striate cortex. Empirically, the surface N40 appears in association with a CSD configuration which includes current sinks within the thalamorecipient (stellate) subdivisions of lamina 4C and a large current source extending considerably below 4C. Dipole ensemble contributions to the CSD profile were computed and compared to physiological data from this region. Small asymmetries in activation of model stellate laminae were sufficient to produce substantial open field contributions. However, the best fit with empirical CSD profile was found when the simulation included contributions from thalamocortical axons, along with both open and closed field contributions from dual stellate cell sublaminae. High-resolution CSD profiles were shown to be interpretable when computational artifacts characteristic of closed and open fields were identified using a series of differentiation grids.

Key words: Current source density – Visual evoked potentials – Striate cortex – Dipole models – Monkey

Correspondence to: C.E. Tenke, Department of Biopsychology, Box 50, NYS Psychiatric Institute, 722 W168 St., New York, NY 10032, USA

Introduction

Synchronous activation of afferents to a cortical region produces an intracortical field potential distribution, or depth profile, that is characteristic of both the stimulus parameters and the anatomical organization of the region. Because of the proportionality between current and voltage in a conductive medium (i.e., Ohm's law), the second spatial derivative of the field potential profile provides an estimate of local net transmembrane current flow. This method is known as current source density (CSD) analysis (Nicholson 1973). The second spatial derivative is usually estimated from voltage samples measured from discrete locations using a finite approximation method (Freeman and Nicholson 1975).

Implementation of CSD analysis within a volume of tissue requires a three-dimensional electrode array or multiple penetrations of the region under analysis. A more practical one-dimensional method may be used with voltage profiles derived from recordings taken along a single axis (Freeman and Stone 1969; Freeman and Nicholson 1975) if three assumptions are satisfied: (1) conductivity in the sampled dimension is approximately isotropic; (2) the principal axis of current flow is parallel to the sampling axis; and (3) the field potential profile does not vary appreciably within a circumscribed region perpendicular to the sampling axis (i.e., there is no cur-

rent flow normal to the sampling axis). These assumptions appear to be reasonable for cortical regions studied to date (Freeman and Nicholson 1975; Hoeltzell and Dykes 1979; Muller-Preuss and Mitzdorf 1984; Mitzdorf 1985; Holsheimer 1987). One-dimensional CSD analyses have proven to be useful in delineating the intracortical timing and distribution of neural activity, as well as for clarifying the neural basis of surface-recorded evoked potentials (Kraut et al. 1985; Mitzdorf 1985; Arezzo et al. 1986; Cauller and Kulics 1988; Schroeder et al. 1990, 1991, 1992; Steinschneider et al. 1992).

Two principal factors influence the accuracy with which CSD analysis can be related to the activation of underlying neural elements: (1) Noise. CSD analysis is highly susceptible to waveform amplitude variability, which must be reduced to the extent possible by adequate recording and averaging techniques. The development of multicontact electrodes (Prohaska 1979; Barna et al. 1981; Mitzdorf 1987) enhances the reliability of the CSD by eliminating the "state-related" variability encountered when profiles are produced by a single electrode which is moved between samples. (2) Spatial resolution. Even when reliable and noise free, the spatial resolution of CSD is restricted by technical limitations on sampling precision and density (e.g., feasible multicontact electrode spacing) and by computational algorithm (e.g., 5-point vs 3-point approximations of the second derivative). Moreover, since CSD is a macroscopic density function, it is presumed that the extracellular sources and sinks are themselves continuous (Nicholson and Freeman 1975). This becomes a problem when, for example, high-resolution recordings inadvertently isolate single units. Although data complicated by these problems may still be examined using CSD techniques, artifacts related to spatial resolution must be identified or discounted.

Concern for the effects of random fluctuations (state and measurement noise) and spatial discontinuities (physiological noise, including occasional isolation of unit activity) has prompted many investigators to adopt procedures which protect the formal validity of the CSD by minimizing the contribution of extremely focal processes (Freeman and Nicholson 1975; Rappelsberger et al. 1981; Mitzdorf 1985; Cauller and Kulics 1988, 1991). These include the deliberate use of low-impedance electrodes, computational smoothing of the profile prior to CSD analysis, the use of a 5-point (or greater) formula for calculation of CSD values, and the use of a wider differentiation grid than the available spatial sampling interval (e.g., next-nearest neighbor). These procedures reduce measurement noise and result in simpler CSD profiles by excluding or attenuating abrupt changes in the vicinity of any single electrode. However, the resulting loss of spatial resolution restricts the capacity of the CSD to delineate the impact of important structural features, such as laminar and sublaminar borders.

The importance of optimizing the spatial resolution of CSD analysis and of understanding the spatial limitations of this procedure is illustrated by empirical studies of neural contributions to the surface-recorded visual evoked potential (VEP) in the monkey. Laminar recordings using multichannel electrodes with contact spacings of 75 or 100 μm have shown that the subdivisions of lamina 4C in the macaque contribute to the surface flash-VEP N40 (Kraut et al. 1985; Schroeder et al. 1990, 1991) and to the pattern VEP N50 component (Schroeder et al. 1991). In the flash-evoked laminar activity profile, the N40 attains its maximum negative amplitude within lamina 4 and undergoes polarity inversion superficial to lamina 5. The concomitant CSD profile shows a current sink/source configuration, with the sink maximal in amplitude within 4C, and the current source extending throughout the deeper laminae, often down to the white matter. Occasionally, a second source may be seen immediately above the maximal sink in 4C. This sink/source configuration is interpreted as reflecting combined depolarization of afferent terminals and postsynaptic (stellate) cells (Kraut et al. 1985; Schroeder et al. 1991). However, the relative contributions of these elements have not been determined. Further, while there is evidence that stimulus-dependent differential activation of the parvo- and magnorecipient subdivisions of lamina 4C can be resolved in CSD profiles (Givre et al. 1991), the factors which govern these effects are not yet fully delineated.

The proposition that stellate cells and thalamic afferents contribute to surface VEP is contrary to traditional views on VEP generators. The stellate cells within lamina 4 have been considered to be closed field generators, by virtue of their symmetric processes (Lorente de No 1947), and thus to contribute little to the surface responses (Creutzfeldt and Houchin 1974). Due to cancellation and temporal scatter, presynaptic contributions to the surface VEP are also generally viewed as meager, if present at all (Mitzdorf 1985). These assumptions, although widely held, have not been adequately tested or modeled.

Although physiological studies alone are unlikely to resolve these issues, computer models can be produced to provide crucial information about the influence of spatial resolution on the field potential and CSD profiles produced by a localizable laminar generator that is completely known. In this study, we modeled the contributions of the thalamorecipient (stellate) subdivisions of lamina 4C, and those of their thalamocortical afferents, to the N40 component of the VEP. We then evaluated CSD profiles derived from these simulations to determine which variations provided the best match with empirical data.

Materials and methods

Physiological rationale

The major components of the VEP consist of a surface negative-to-positive transition, with corresponding maxima at 40 and 65 ms (N40 and P65), that abruptly inverts in polarity near the base of lamina 4C. The CSD profile exhibits a pronounced current sink within lamina 4 with a time course comparable with the N40 component. The abrupt inversion of N40 corresponds to a transition from sink to source at the lamina 4/5 border (Kraut et al. 1985; Schroeder et al. 1990, 1991). While the sink spans the two subdivisions of lamina 4C (Schroeder et al. 1991), it may be attenuated

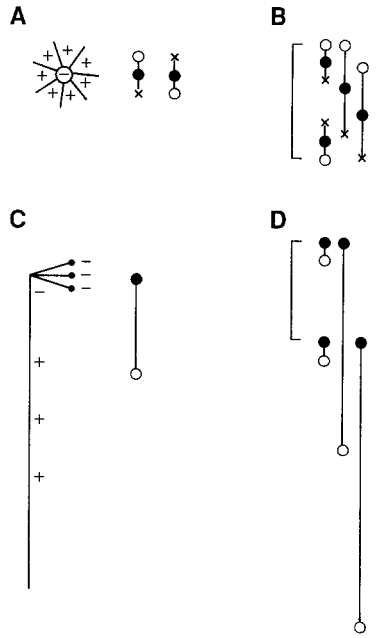

Fig. 1A–D. Generator elements constructed to simulate properties of stellate cell and terminal depolarization. **A** A schematized stellate cell (*left*) consists of a depolarized soma (−) drawing return current from randomly spaced, symmetric dendrites (+). Since large numbers of cells are present, and the activation is transpositionally invariant, only a pair of equivalent dipoles is considered *(right)*, sharing a common sink (shown separated for clarity). Each dipole consists of a sink *(solid circle)* and a source *(open circle)* separated by a dipole length proportional to the size of the cell. For each dipole, the location of the source of a complementary dipole which shared a common sink was also preserved (x, "potential sources") **B** Stellate cell lamina was modeled using an ensemble of individual generator elements. All poles (sinks and both real and potential sources) were confined within 125-μm laminar borders *(bracket on left)*. Generators were randomly distributed within the depth of the lamina as described in the text. The proportion of inverted elements was varied across simulations. **C** Terminal depolarization was modeled as a consistently depolarized region of axon terminals (−) which must draw return current from deeper portions of their respective axons (+). The effective dipole generator *(right)* is thereby a sink *(solid circle)* associated with a deeper source *(open circle)*. **D** Terminal depolarization dipole elements were all oriented in the same direction (sink up), and were combined in the same manner as described for the stellate cell contribution. While sinks were distributed throughout the lamina, sources were allowed to extend below the lamina

(Schroeder et al. 1990) or replaced by a small source (Kraut et al. 1985) in lamina 4Cα when measured at high resolution in some recordings. The N40 sink has a variable, small amplitude in laminae 4A and B (Kraut et al. 1985; Schroeder et al. 1990; 1991). The current source corresponding to N40 begins immediately below the location of the maximal sink, where it abruptly reaches maximal amplitude. This source extends throughout the deeper laminae, and may be traced into the underlying white matter with appropriate electrode placements.

We simulated field potential profiles corresponding to the N40 peak using ensembles of dipole generators arranged to mimic properties of lamina 4C. The dimensions and distributions of these generators were chosen to conform to the spatial dimensions of the sublaminae of 4C of striate cortex and the stellate cells within them (Lund 1984, 1988). Contributions of the remaining laminae, including the superficial subdivisions of lamina 4, were not addressed by this model.

Generator elements

Dipole generators were constructed of monopoles defined by:

$$\Phi(d) = I/4\pi\sigma_d\,|d| \qquad (1)$$

where Φ is the field potential in microvolts, d is the distance in microns of a recording electrode from a given monopole, and σ is the conductivity of the medium (Freeman and Nicholson 1975). Equation 1 is a restatement of Ohm's law in a conductive medium, whereby the resistance offered by the tissue is expressed as a function of distance (d) and conductance (the inverse of resistivity). The amplitude of the injected current (I) was arbitrarily chosen to produce a field potential of 10 μV at a distance of 10 μm from the pole.

The medium was assumed to be isotropic, with a constant conductivity of $3 \times 10^4/\Omega$mm, a value comparable with those reported in physiological studies (Freeman and Stone 1969; Nicholson and Freeman 1975; Nunez 1981). One-dimensional field potential profiles were initially simulated at 10-μm resolution and then resolution was altered in 10-μm increments to 50 or 100 μm for CSD computation, in order to simulate recordings from a multicontact electrode with a 50- or 100-μm intercontact spacing.

Stellate cell activation

Symmetric activation of a stellate cell was simulated by a pair of equivalent dipoles of opposite orientation, aligned parallel to the measurement axis and sharing a common sink (Fig. 1A). We used variable dipole lengths of 20–50 μm to conform to the scale of stellate cells in lamina 4C (Lund 1984, 1988).

Lamina construction

A lamina of dipole elements was constructed by summing the fields produced by a series of concentric rings of dipoles. Rings were constructed with radii of 20–500 μm in discrete, 20-μm increments; the maximum radius is therefore the same order of magnitude

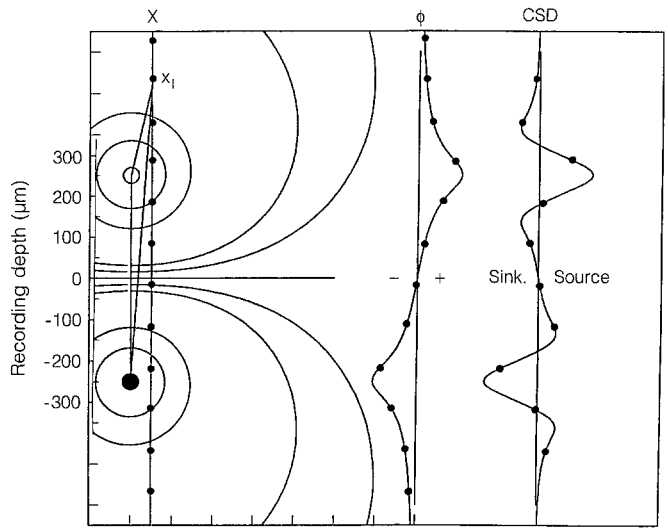

Fig. 2. Field potential profile (Φ) and three-point current source density *(CSD)* computed for a dipole, shown at *left* with a series of isopotential lines. In this example, the dipole length is 500 μm (±250 μm), and the measurement axis (X) is located 50 μm from the dipole axis ($r = 50$ μm for all x). For point x_i, the distances to both contributing poles are illustrated. Values for CSD (x) were computed from the field potential profile $\Phi(x)$ at a 100-μm resolution using Eq. 3 (source on *right;* sink on *left*). One such case is illustrated using *solid circles*

expected of cortical columns. The 20-μm conductive gap surrounding the electrode is consistent with practical (e.g., localized tissue displacement, cell damage) and theoretical (e.g., distributed volume generators) constraints on the application of CSD techniques to physiological profiles (Nicholson 1973). A constant packing density of 1 generator per π μm circumference (40 generators in innermost ring) was maintained for all rings. This value was adequate to produce continuous profiles with acceptable computation times.

Dipole generators were equiprobably positioned within the 125-μm lamina with one constraint: there must be room for the elements of a pair of dipoles of opposing polarity which share a common sink. Each generator thus consisted of a central sink, a source, and a symmetric place-marker, representing the location of the source of the complementary dipole required for precise symmetry (*X*'s in Fig. 1A, B). Dipole lengths were uniformly varied over the range of 20–50 μm. Closed field generators were simulated by inverting 50% of the dipoles in a lamina; open field (asymmetric) laminae were examined by inverting different proportions of dipoles (60, 75, and 100%).

Field potential profiles were computed as a function of displacement along the measurement axis (x) and the eccentricity of each monopole generator from this axis (r). In these, and all subsequent simulations, the total field potential at any point x resulting from N monopoles was computed as:

$$\Phi_T(x, r) = \sum_{i=1}^{N} \Phi_i(d_i) \quad (2)$$

where Φ_i is the contribution of monopole i. Figure 2 illustrates these relationships, as well as the resulting field potential profile.

Contributions from terminal depolarization

In order to model the contributions of terminal depolarization to the lamina 4C profile, it was presumed that: (1) the extracellular sinks corresponding to the depolarization of terminals within a sublamina are confined to the 125-μm sublamina; (2) the circuit-closing sources for the terminal must arise exclusively from deeper portions of each thalamocortical fiber. Based on the conduction velocity of these axons, and the random state of depolarization expected for a given fiber, dipole lengths were varied over the range of 20–500 μm (Fig. 1C, D). Since all dipoles were oriented with sinks superficial to their sources, source locations ranged from upper portions of the lamina to 500 μm below it. Dipoles were spaced radially, as described for the stellate model above.

CSD computation

For each field potential profile, data resolution was altered in 10 μm increments to produce three sample intervals for the computation of CSD profiles: 50, 100, and 200 μm. One-dimensional CSD estimates were then computed using three widely used procedures (Freeman and Nicholson 1975): (1) consecutive 3-point, (2) next-nearest-neighbor 3-point, and (3) a 5-point formula. CSD profiles were expressed in microvolts per millimeter for 100-μm computations after removal of a lumped constant that includes conductivity. Three-point estimates were produced at each location (x) using the following formula:

$$\mathrm{CSD}(x) = -\left[\frac{\Phi(x-h) - 2\Phi(x) + \Phi(x+h)}{h^2}\right] \quad (3)$$

where h is the intercontact separation. The numerator of Eq. 3 was equated with the 3-point 100-μm CSD by applying a descaling factor equal to the square of the ratio of the differentiation grids [e.g., at 200 μm the ratio is $4 = (200\ \mu m/100\ \mu m)^2$].

The 5-point CSD profiles were computed by

$$\mathrm{CSD}(x) = -\left[\frac{2\Phi(x-2h) - \Phi(x-h) - 2\Phi(x) - \Phi(x+h) + 2\Phi(x+2h)}{7h^2}\right] \quad (4)$$

Since the 5-point procedure spans the same number of 100-μm points as the next-nearest-neighbor, 3-point computation, the two computations were descaled by the same factor (i.e., 4).

Results

Closed field profile

The closed field lamina (50% inverted dipoles) produced a field potential profile characterized by a pronounced negativity at recording sites within the lamina, and a low-amplitude positivity external to the laminar borders. The abrupt transition is characteristic of a closed field. Descriptive statistics for the point generators comprising the innermost ring (innermost 40 dipoles) were as follows: (1) sinks were distributed from 41.6 μm above to 36.2 μm below the middle of the lamina and a mean offset of 1.99 μm (SD 17–13; skewness 2.97; median 0.65 μm); (2) sources were distributed with a range of 1.7–62.5 μm in either direction from the center of the lamina, with mean offsets of 36.7 μm (17.18 SD; skewness 0.408); (3) dipole length varied from 20.2 to 47.1 μm, with a mean of 34.11 (SD 8.35; skewness 0.10). The continuity and symmetry of the field potential distribution was further improved by the contributions of the remaining rings, as is evident from the field potential profile they produced (Fig. 3A, bold trace).

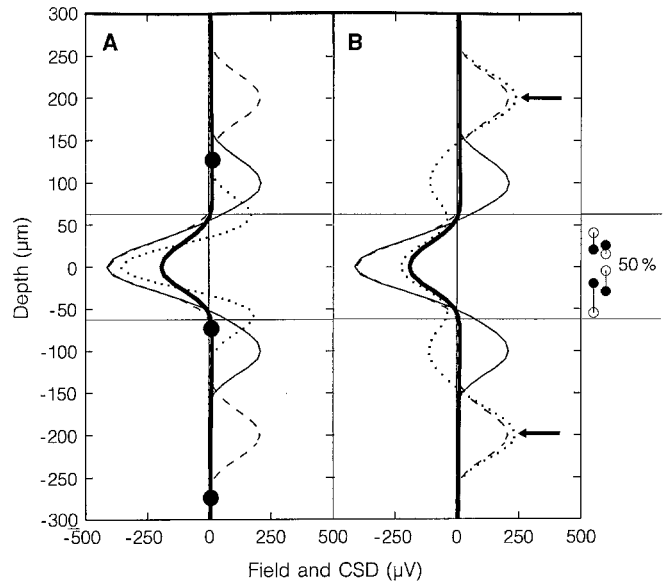

Fig. 3A, B. Field and CSD profiles of simulated stellate lamina composed of closed field generators (50% inverted). *Vertical,* depth in microns; *horizontal,* amplitude in microvolts. Laminar borders are indicated by *horizontal lines.* Sample dipoles are shown on the *right* of the figure sources (*open solid,* sinks) **A** Field potential *(bold line)* and 3-point CSD (*negative,* sink; *positive,* source) with differentiation grids of 50 *(dotted lines),* 100 *(solid),* and 200 μm *(dashes).* In this and following figures, CSD amplitudes are scaled to eliminate the denominator of Eq. 3 at 100 μm. The other methods are scaled as described in the text. *Solid dots* on the field potential indicate a 200-μm electrode placement at which the closed field is undetectable. **B** Field potential and CSD profiles computed at 100 μm resolution using 3-point *(solid),* next-nearest-neighbor *(dashes),* and 5-point estimates *(dotted).* For the latter two methods, sources are misallocated to the same locations *(arrows)*

The impact of differentiation grid on the capacity of the CSD to appropriately localize a closed field generator is illustrated in Fig. 3A. All 3-point CSD methods (50, 100, and 200 μm differentiation grids) appropriately detected a sink centered within the lamina. The two low-resolution grids yielded comparable magnitude estimates for the flanking sources, which are slightly larger than for the 50-μm grid. However, the locations of these sources varied with the differentiation grid utilized. For all differentiation grids, the location of the source peak was displaced (misallocated) precisely one differentiation interval from the negative field-potential peak. Thus, source localization was unrelated to either laminar borders or the distribution of real sources.

At the lowest resolution, 200 μm, the flanking sources were separated from the sink by a CSD null region. Thus, when the differentiation grid and spatial sampling density were both 200 μm (e.g., solid dots in Fig. 3A), all CSD features vanished with many possible alignments of the recording contacts. The CSD is capable of reliably detecting and localizing the sources using higher resolution sampling, but fails when spatial sampling is inadequate. Figure 3B illustrates a comparison of CSD profiles computed from a sampling interval of 100 μm using 3-point (100-μm grid), 3-point next-nearest-neighbor (200-μm grid), and 5-consecutive-point formulae. In keeping with the spatial smoothing effect of the 5-point formula, the central sink is attenuated and extended beyond the borders of the generating lamina. However, this formula does not prevent the misallocation of sources (see arrows); the sources are not attenuated, but are displaced to the same location as in the case of the next-nearest-neighbor, 3-point calculation.

Open field profile

Variations in the proportion of inverted dipole elements transformed the closed field lamina into an open field generator. The field potential profile obtained when 75% of the dipoles were inverted is illustrated in Fig. 4A. The field potential external to the lamina increased in amplitude approximately linearly as the borders were approached. Within the lamina, the closed field contribution was evidenced by a characteristically abrupt acceleration in the amplitude of the field potential. The primary characteristics of the closed field (50%) CSD profile are identifiable in the 75% inverted profile (Fig. 4A). Again, the maximum sink is adequately localized by the 3-point formula with all grids. The location of the superficial source also varied with the differentiation grid, whereas its amplitude increased slightly as the contact spacings were increased from 50 to 200 μm. The location of the deep source was also influenced by the same form of misallocation. Both sources were larger with 100- and 200-μm spacings than at 50 μm. However, two additional properties emerge: (1) the deep source is substantially larger than the superficial one for all grids; (2) the spatial extent of the central sink and deep source distinctly increase with the use of a wider differentiation grid, in contrast to the superficial source.

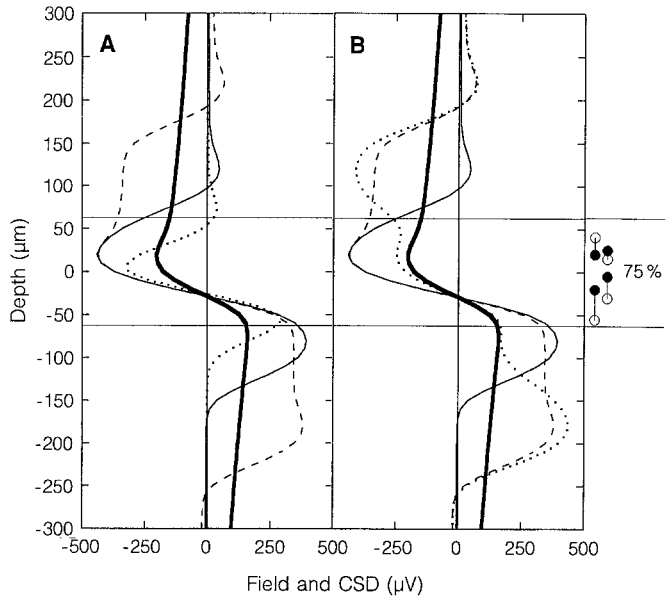

Fig. 4A, B. Stellate lamina with 75% inverted dipoles. **A** Field potential profile and 3-point CSD at 50, 100, and 200 μm (as in Fig. 3A). **B** Field potential and CSD profiles computed at 100 μm resolution using 3-point, next-nearest-neighbor, and 5-point estimates (as in Fig. 3B)

The sources calculated by the 5-point, 100-μm formula peaked at the same locations as did those produced by the 3-point, 200-μm calculation (Fig. 4B), but, as in the case of the closed field generator, these were displaced further from the lamina than with the 100-μm, 3-point calculation. Both the 5-point and 200-μm formulae introduced superficial and deep artifacts at 100 μm, but the 5-point distortion was greater. The 5-point, 100-μm method produces an additional problem for the interpretation of the open field contributions of the lamina in that it also produced a substantial attenuation of the actual current sink inside the lamina. Thus, the 5-point CSD profile generates large errors in CSD features.

Stacked laminae

When two simulated 75% inverted dipole laminae were juxtaposed, the resulting field potential profile reflected the superposition of contributions from each lamina. Figure 5A illustrates the field and 3-point CSD profiles obtained for two adjacent pairs of 125-μm laminae (120-μm center-to-center offset; 5-μm overlap). As with a single simulated lamina, the 50-μm CSD appropriately localized the real current sink within each lamina, and produced spurious sources external to the (combined) laminae. The superficial sink and deep source were not as well localized at lower resolution, and extend considerably beyond the external laminar borders. However, the relative misallocation of these features was reduced compared with a single lamina (compare Fig. 5A with 4A). In addition to these CSD features, a real source emerged at the common laminar border at 50 and 100 μm resolution. This source disappeared at 200 μm CSD resolution, and reflects the requirement that sources cannot extend beyond their own laminar border.

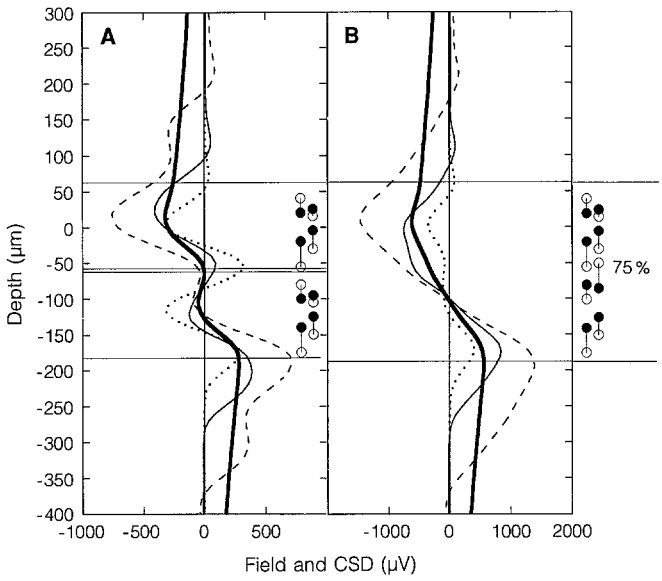

Fig. 5A, B. Two 125-μm-wide, open field (75%) laminae, with centers separated by 120 μm. **A** Field potential profile and 3-point CSD at 50, 100, and 200 μm (as in Fig. 3A). Laminar borders indicate the 5-μm overlap of the two laminae. **B** A single 250-μm-wide, open field (75%) lamina. Field potential profile and 3-point CSD at 50, 100, and 200 μm (as in Fig. 3A)

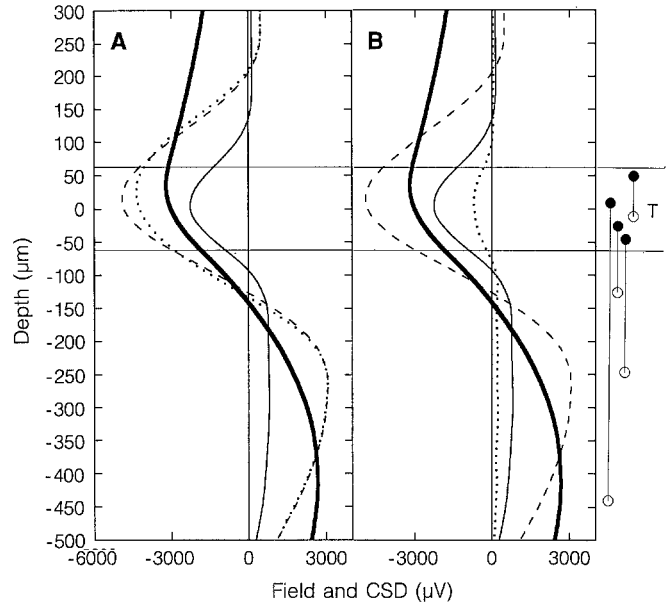

Fig. 6A, B. Terminal field (*T*) lamina, with sinks distributed over 125 μm, showing sink borders and sample dipoles. **A** Field potential and CSD profiles computed at 100 μm resolution using 3-point, next-nearest-neighbor, and 5-point estimates (as in Fig. 3B). **B** Field potential profile and 3-point CSD at 50, 100 and 200 μm (as in Fig. 3A)

In spite of the misallocation and smearing, it is apparent that even the low-resolution CSD retains the capacity to detect and approximately localize the characteristics of open field generators. When the width of a single 75% open field lamina was increased to 250 μm (Fig. 5B), all CSD methods localized a sink peak within the superficial half of the lamina, and a deep source near the lower laminar border. For the highest resolution CSD (50 μm), the lamina is separable into an upper portion, characterized by a source, and a lower portion, characterized by a sink, with peaks in proximity to the laminar borders. Again, at all resolutions, sources due to the closed field component were comparable in amplitude and misallocated by one sampling interval across the upper laminar border. The real sources and sinks (the open field component) grew in amplitude and were smeared beyond the laminar borders when low-resolution methods were used; they were considerably larger than the closed field artifacts.

Contributions from terminal depolarization

For the terminal depolarization model, field potential amplitudes were an order of magnitude greater than those encountered with the closed field laminae, owing to the smaller amount of cancellation. Additionally, the spatial range occupied by the generator elements in the terminal depolarization model was over 5 times greater than that occupied by the elements in a single closed field lamina. All CSD calculations (see Fig. 6A) localized a well-defined sink which peaked within the lamina. At high (50 μm) resolution, a real source was seen uniformly distributed below the lamina, with minimal misallocation of sources above the lamina. As resolution decreased, smearing of the sink across the laminar borders increased, the real source below the lamina appeared less uniform, and misallocation of sources above the lamina increased. As in the open field laminae previously described, the real source and sink had a higher measured amplitude when computed using the lowest resolution. In contrast, the accuracy of localization was improved by using the highest resolution available.

Matching physiological requirements

As is evident in Figs. 3–6, none of the variations of a closed field lamina alone are adequate to describe the deep sources typical of the N40 profile. However, the fit was improved by collocation of stellate closed field (50% inverted) and terminal depolarization models (Fig. 7A). A necessary requirement for a good fit is a reduction in the amplitude of the terminal depolarization contribution. This is acceptable on anatomical grounds, since there is substantially less contiguous surface area to support spatial and temporal summation in axon terminals than on postsynaptic sites (somatic and dendritic) on neurons in lamina 4. As in the simpler models, the use of a wide differentiation grid increased the amplitude, and thereby the detectability, of CSD features, but led to a misallocation of real features across laminar borders. Variations in the amplitude and composition of adjacent laminae were only found to improve the fit when one or both sublaminae were constructed as open field generators. Figure 7B depicts results obtained using a com-

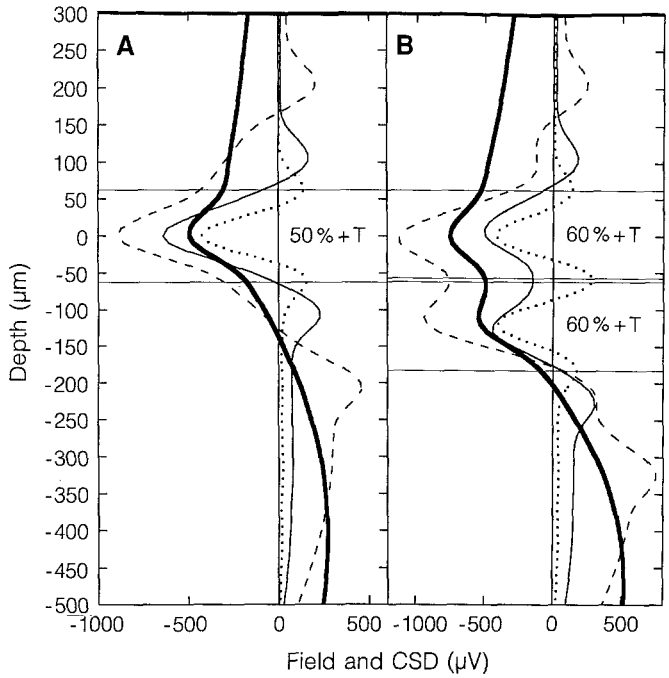

Fig 7A. Composite of terminal depolarization (*T*) (scaled to 10% amplitude) and closed field (50% inverted) laminae. Field potential profile and 3-point CSD at 50, 100, and 200 μm (as in Fig. 3A). **B** Two composites of terminal depolarization (scaled to 10% amplitude) and open field (60% inverted) laminae, with centers separated by 120 μm. Field potential profile and 3-point CSD at 50, 100, and 200 μm (as in Fig. 3A)

posite model consisting of two stacked open field (60% inverted) stellate sublaminae, each associated with a component representing terminal depolarization. The models depicted in Fig. 7 approximate the key features of the physiological data. The field potential above the laminae has a linear falloff, and abruptly increases in amplitude at the upper border. The models also mimic the distributed source extending below, including the maximum at the lower border of lamina 4. Both of the composite models are consistent with a misallocated source measured immediately superficial to the maximum sink. Only the stacked model (Fig. 7B) can account for sinks in both lamina 4Cα and 4Cβ.

Discussion

CSD analysis is used to infer the timing and predominant direction of transmembrane currents associated with neural excitation or inhibition, and for defining the intracortical processes that contribute to surface-recorded, event-related potentials (Arezzo et al. 1986; Vaughan and Arezzo 1988; Schroeder et al. 1990). Although CSD data must be interpreted on the basis of the anatomical and biophysical properties of each region studied (e.g., Mitzdorf 1985), the available data on intracortical synaptic architecture are often insufficient to clearly differentiate between alternative physiological hypotheses. Computer simulations can model hypothetical generator configurations in a way that may be tested against physiological data. If a hypothetical generator is properly simulated, but yields CSD profiles which fail to match key features of the physiological data, the proposed generator hypothesis must be rejected or modified. If the profiles match, details of the modeled distribution may underscore or clarify features of the physiological data.

Closed field generators

The principal heuristic value of our closed field model (Figs. 3, 4) of uniform activation of stellate neurons is the finding of a consistent misallocation of current sources beyond meaningful physiological boundaries. Our results demonstrate that it is possible to identify closed field activity in an intracortical profile by: (1) the presence of abrupt accelerations in an otherwise linear field potential gradient; (2) the presence of localized artifacts of valid CSD features that change their apparent location as the differentiation grid is varied; (3) constant-amplitude CSD features across a series of differentiation grids.

The present model was designed to enforce strict laminar boundary requirements, which allows the reliable separation of real and artifactual CSD features. However, our use of randomized dipole length and placement avoided the production of unrealistically abrupt transitions at the laminar boundaries. The misallocation of sources found for this closed field model are consistent with those found for our preliminary models, in which the laminar borders themselves were constructed statistically (Tenke et al. 1988; Tenke and Schroeder, unpublished observations).

Closed field artifacts versus passive features

Within a CSD profile, a source or sink may be identified as active or passive, in accordance with processes presumed to be responsible for its generation. An "active sink" reflects the macroscopic summation of localized excitatory postsynaptic potentials (EPSPs) or action potentials, whereas a passive source represents the path by which circuit-closing current flows from adjacent portions of the neuronal membrane. Conversely, inhibitory postsynaptic potentials (IPSPs) may be associated with "active current sources" flanked by passive current sinks (Schroeder et al. 1990). Since both active and passive transmembrane current flow require a continuous cell membrane, neither can exceed the dimensions of the responding neural elements. By contrast, the location of a closed field artifact can violate this physiological constraint, since it is introduced by sampling and computational methods.

The location at which current closure occurs is discretely defined in relation to the active site in our closed field generator model. However, the corresponding CSD profile invariably allocates the current return to an adjacent, artifactual location. The origin of the misallocated sources is real; source and sink contributions numerically cancel each other out within a closed field generator, leaving a greater number of unopposed sources at positions offset from the middle of the lamina. Despite their

real origin, the locations of closed field sources are artifactually determined by the spatial sampling used in computing the CSD, and thus do not conform to structure or physiology.

Closed field artifacts in the CSD are also distinct from those produced whenever a recording contact is aligned near an isolated, spherical generator (see Fig. 2). In the latter case, current is actually lost to the dimension sampled; the profile varies with radial displacement from the generator. Such artifacts diminish as the radius of the generator is increased, while closed field artifacts do not (Nicholson and Freeman 1975; Tenke et al. 1988). These misallocated, closed field features are due to the edge-detecting properties inherent in the computation of a second derivative. Our models suggest that the misallocation is predictably related to the sampling technique employed in the analysis.

Open field generators

Since open fields are measurable over large distances, they may be identified using a wide differentiation grid. The cost of this approach is that the locations of the sources and sinks underlying them will be smeared external to their true location. However, it should also be noted that the integrity of a wide, continuous dipole lamina may be obscured if a differentiation grid is used that is appreciably smaller than the thickness of the generator lamina (Fig. 5B). The cancellation of the local field potential near the center of the lamina leads to an accumulation of uncancelled sources and sinks near opposite halves of the lamina. This effect derives from the algebraic summation of microscopic currents within the macroscopic region sampled, and does not reflect differential activity at the border itself.

Open field generators within lamina 4 are not prominently affected by this summation, since the sublaminae, and the distinctly activated cells within them, are smaller than available sample intervals. Large pyramidal cells, however, may produce this pattern in an exaggerated form. It would be expected that resultant generators produced by pyramidal cell activation may appear as a source-sink pair centered about a current null. The routine use of two grids (3-point and next-nearest-neighbor) provides a method for identifying misallocated features caused by inadequate spatial sampling of closed field contributions. This approach also provides a computationally independent validation of open field features, since the outlying recording contacts differ for the two CSD computations.

Physiological relevance

The lamina 4C sink that corresponds to N40 is separable into at least two components: (1) a presynaptic open field, drawing current return from a source distributed deep to it; and (2) a postsynaptic mixed contribution (open and closed field), drawing return current from adjacent sources. Despite the collocation of the open and closed field sinks, they are discriminable in physiological CSD profiles by their misallocation patterns.

Our data indicate that stellate cell contributions to the field potential profile are most prominent locally, corresponding to the closed field contribution. The closed field sinks within lamina 4C dominate the high-resolution CSD. While passive current return is drawn from contiguous locations, the CSD misallocates these sources to the nearest electrode location available to the computation. However, the nuances of the CSD profile through lamina 4Cα vary considerably, depending on the inter-contact spacing of the electrode and its alignment within the lamina. For example, the sink may appear to be locally attenuated (Schroeder et al. 1990) or replaced by a source which has been misallocated from the location of the maximum sink (Kraut et al. 1985). As a result of the diminished closed field contribution at lower resolution (150 μm), the sink may also appear unattenuated throughout lamina 4C (Schroeder et al. 1991).

From our simulations, it is clear that no postsynaptic lamina 4 generator can explain the extended subgranular source corresponding to N40. The only postsynaptic process that could match the data would be local depolarization of apical dendrites of deep pyramidal neurons within lamina 4C, with hyperpolarization of the cell bodies and proximal portions of the apical dendrites. This pattern would require either: (1) EPSPs on the apical dendrites within lamina 4, with predominant current return to the proximal dendrites and cell bodies within the subgranular laminae; (2) deeply placed IPSPs drawing a return current from lamina 4C; or (3) nonsynaptic depolarization of the apical dendrites via the extracellular medium. These possibilities do not seem consistent with the known anatomy and physiology of primate striate cortex. The simulations strongly suggest that the early subgranular source represents the current return from more proximal segments of thalamocortical axons during terminal depolarization.

The contribution of presynaptic elements to the VEP has previously been discounted a priori on physiological grounds (Mitzdorf 1985), owing to temporal dispersion of the afferent volley from cancellation of the diphasic waveform associated with terminal depolarization and subsequent repolarization. However, the slower depolarization properties of axon terminals would enhance the degree of temporal integration of an incoming volley. Furthermore, stroboscopic flash stimulation produces sufficiently synchronous firing in the thalamocortical projections of lamina 4C to maximize the magnitude of these contributions (Schroeder et al. 1989b).

The present model was restricted to the study of lamina 4C and its afferents, since these represent the most spatially discrete generators within striate cortex. We have not incorporated the contributions of laminae 4A and 4B. While physiological evidence indicates a small and inconsistent contribution from these laminae when viewed at high resolution (Schroeder et al. 1990; Kraut et al. 1985), a sink may be seen throughout lamina 4 when viewed at low resolution (Schroeder et al. 1991; 150 μm). Supragranular contributions have also been omitted in the present model. Since the supragranular

CSD profile varies with behavioral state (Schroeder et al. 1989a; Cauller and Kulics 1988, 1991), extensions of the model which include these contributions will be particularly useful for interpreting the mechanisms underlying cognitive processes.

Relation of intracortical activity to surface-recorded evoked potentials

Modeling the intracortical generators to conform with empirical CSD data provides a method for evaluating the relative contributions of specific features of the intracortical laminar activation pattern to the surface-recorded potentials. In cases where the contribution to the dipolar, far-field recording can be ascribed to specific laminar locations, and by inference to specific cell populations, it becomes possible to interpret some aspects of surface-recorded activity in terms of specific features of intracortical physiology. Thus, in the example employed in this paper, we have shown that the main contributions to the initial surface negative component (N40) of the monkey VEP can be generated by a combination of presynaptic activation of the axon terminals of the thalamocortical afferents and EPSPs on the stellate cells within lamina 4C. A thalamocortical origin has also been proposed for the N8 component of the auditory evoked potential (EP; Steinschneider et al. 1992). This conclusion refutes the generally held notion that only cortical pyramidal cells possess the necessary geometry and activation pattern to act as open field generators (Lorente de No 1947; Creutzfeldt and Houchin 1974).

Scalp recordings of the electromagnetic signals generated within the brain provide the only available noninvasive method for gaining information on the dynamic neural activity associated with sensory, motor, and cognitive processes. Although most cortical, and many subcortical, structures generate signals that can be recorded at the scalp, these potentials represent only the dipolar component of the complex multipolar current generators within each active structure. In view of the complex laminar pattern of current sources and sinks within a cortical generator, the validity of the equivalent dipole model may not be self-evident. This is, however, a consequence of the properties of multipolar electrical field propagation, in which the higher order terms decrease with distance much more rapidly than the dipolar term. This theoretical consideration is substantiated by empirical data. Recordings obtained from several cortical regions demonstrate a transcortical polarity inversion characteristic of dipolar "open field" generators (Arezzo et al. 1986).

The dipolar property has proven useful in developing methods for localization of intracranial generators of surface potentials (e.g., Scherg 1989; Nunez 1990). In evaluating the contributions of specific regions or cellular populations within an active structure to the equivalent dipolar generator, it is crucial that the microstructure and physiological properties of the tissue be appreciated. These generators ultimately represent a weighted sum of the contributions of all transmembrane currents within the active structure. Since CSD profiles detail the spatiotemporal pattern of activation within a generator, it would be valuable to relate them to the major features of surface-recorded potentials or magnetic fields. An elaboration of the CSD methods described here shows promise for dissociating local (cancelled and closed field) activity from the volume-conducting (open field) activity produced by the lateral geniculate nucleus, which contributes to the surface N25 component (Tenke and Schroeder 1991; Schroeder et al. 1992).

Strengths and limitations of the CSD

In principle, the sources and sinks derived from one-dimensional CSD profiles may be matched to anatomical landmarks (e.g., cortical laminae or sublaminae), thus allowing inferences to be drawn regarding the neuronal subpopulations and processes responsible for the surface waveform. However, differences between the anatomical and physiological properties of cortical regions and variations in their spatiotemporal patterns of physiological activation require considerable flexibility when studied using the continuous model of laminar and sublaminar transmembrane current flow which is implicit in the application of the CSD. If the spatial sampling resolution is too low, it is impossible to adequately represent variations having a high spatial frequency, thereby impairing efforts at relating the physiological patterns of current sources and sinks to the anatomy of the tissue under study. As spatial resolution is increased, inaccuracies due to technical factors, which include computational noise in the approximation of the second derivative, local tissue deformation, or limitations in electrode construction, affect the validity of the CSD, even if all formal requirements are met.

The ability to reliably differentiate between physiological and artifactual contributions is an essential requirement for the valid application of the CSD technique. For optimal utility, the field potential profile must be measured at the highest resolution that is technically possible. At extremely high resolution, the edge-detecting properties of the second derivative still provide advantages for the localization of sublaminar generators. However, the technical and formal limits of the CSD must be also be addressed. While an intimate familiarity with the properties of both tissue and technique is crucial to the interpretation of a high-resolution profile, the CSD technique has the capacity to provide insights into the activation patterns of ensembles of intracortical neuronal populations at sublaminar dimensions. As illustrated by this report, these empirical data may then be formalized and evaluated using simulations based upon specific anatomical hypotheses.

Acknowledgements. The authors would like to thank Drs. Mitchell Steinschneider and James Towey for their helpful comments. This work was supported by grants MH36295 and MH06723 from NIMH.

References

Arezzo JC, Vaughan HG Jr, Kraut MA, Steinschneider M, Legatt AD (1986) Intracranial generators of event-related potentials in

the monkey. In: Cracco R, Bodis-Wollner B (eds) Evoked potentials. Liss, New York, pp 174–189
Barna JS, Arezzo JC, Vaughan HG Jr (1981) A new multielectrode array for the simultaneous recording of field potentials and unit activity. Electroencephalogr Clin Neurophysiol 52:494–496
Cauller LJ, Kulics AT (1988) A comparison of awake and sleeping cortical states by analysis of the somatosensory-evoked response of postcentral area 1 in rhesus monkey. Exp Brain Res 72:584–592
Cauller LJ, Kulics AT (1991) The neural basis of the behaviorally relevant N1 component of the somatosensory-evoked potential in SI cortex of awake monkeys: evidence that backward cortical projections signal conscious touch sensation. Exp Brain Res 84:607–619
Creutzfeldt O, Houchin J (1974) Neuronal basis of EEG waves. In: Remond A (ed) Handbook of electroencephalography and clinical neurophysiology, vol 2C. Elsevier, Amsterdam, pp 5–55
Freeman JA, Nicholson C (1975) Experimental optimization of current source density technique for anuran cerebellum. J Neurophysiol 38:369–382
Freeman JA, Stone JA (1969) A technique for current density analysis of field potentials and its application to the frog cerebellum. In: Linas R (ed) Neurobiology of cerebellar evolution and development. American Medical Association, Chicago, pp 42–430
Givre SJ, Schroeder CE, Bazarian RA, Arezzo JC (1991) Timing and laminar distribution of activity evoked by white light versus color in VI and V4 of the awake macaque. Soc Neurosci Abstr 17:1568
Hoeltzell PB, Dykes RW (1979) Conductivity in the somatosensory cortex of the cat – evidence for cortical anisotropy. Brain Res 177:61–82
Holsheimer J (1987) Electrical conductivity of the hippocampal CAl layers and application to current-source-density analysis. Exp Brain Res 67:402–410
Kraut MA, Arezzo JC, Vaughan HG Jr (1985) Intracranial generators of the flash VEP in monkeys. Electroencephalogr Clin Neurophysiol 62:300–312
Lorente de No RA (1947) A study of nerve physiology. (Rockefeller Institute for Medical Research, study 132) Rockefeller Institute, New York, pp 389–477
Lund JS (1984) Spiny stellate neurons. In: Peters A, Jones EG (eds) The cerebral cortex, vol 1. Plenum, New York, pp 255–304
Lund JS (1988) Anatomical organization of macaque monkey striate visual cortex. Annu Rev Neurosci 11:253–288
Mitzdorf U (1985) Current source-density method and application in cat cerebral cortex: investigation of evoked potentials and EEG phenomena. Physiol Rev 65:37–100
Mitzdorf U (1987) Properties of the evoked potential generators: current source-density analysis of visually evoked potentials in the cat cortex. Int J Neurosci 33:33–59
Muller-Preuss P, Mitzdorf U (1984) Functional anatomy of the inferior colliculus and the auditory cortex: current source density analysis of click-evoked potentials. Hear Res 16:133–142
Nicholson C (1973) Theoretical analysis of field potentials in anisotropic ensembles of neuronal elements. IEEE Trans Biomed Eng 20:278–288
Nicholson C, Freeman JA (1975) Theory of current source-density analysis and determination of conductivity tensor for anuran cerebellum. J Neurophysiol 38:356–368
Nunez PL (1981) Electric fields of the brain: the neurophysics of EEG. Oxford University Press, Oxford, New York
Nunez PL (1990) Localization of brain activity with electroencephalography. Adv Neurol 54:39–65
Prohaska O, Pacha PF, Pfunder P, Petsche HA (1979) 16-fold semimicroelectrode for intracortical recording of field potentials. Electroencephalogr Clin Neurophysiol 47:629–631
Rappelsberger P, Pockberger H, Petshe H (1981) Current source density analysis: methods and application to simultaneously recorded field potentials of rabbit's visual cortex. Pflugers Arch 389:159–170
Scherg M (1989) Fundamentals of dipole source potential analysis. In: Hoke M, Grandori F, Romani GL (eds) Auditory evoked magnetic fields and potentials. Adv Audiol 6:2–30
Schroeder CE, Givre SJ, Tenke CE, Arezzo JC, Vaughan HG Jr (1989a) Visual processing in awake monkeys under active and passive conditions. Soc Neurosci Abstr 15:119
Schroeder CE, Tenke CE, Arezzo JC, Vaughan HG Jr (1989b) Timing and distribution of flash-evoked activity in the lateral geniculate nucleus of the alert monkey. Brain Res 477:183–195
Schroeder CE, Tenke CE, Givre SJ, Arezzo JC, Vaughan HG Jr (1990) Laminar analysis of bicuculline-induced epileptiform activity in area 17 of the awake macaque. Brain Res 515:326–330
Schroeder CE, Tenke CE, Givre SJ, Arezzo JC, Vaughan HG Jr (1991) Striate cortical contribution to the surface-recorded pattern-reversal VEP in the alert monkey. Vision Res 31:1143–1157
Schroeder CE, Tenke CE, Givre S (1992) Subcortical contributions to the surface-recorded flash-VEP in the awake macaque. Electroencephalogr Clin Neurophysiol 84:219–231
Steinschneider M, Tenke CE, Schroeder CE, Javitt DC, Simpson GV, Arezzo JC and Vaughan HG Jr (1992) Cellular generators of the cortical evoked potential initial component. Electroencephalogr Clin Neurophysiol 84:196–200
Tenke CE, Schroeder CE, Arezzo JC, Vaughan HG Jr (1988) Computational and sampling considerations in the analysis of localized and distributed processes by one dimensional current source density techniques. Soc Neurosci Abstr 14:1252
Tenke CE, Schroeder CE (1991) Lateral geniculate nucleus (LGN) response to flash: current source density (CSD) and principal components (PCA) analyses. Soc Neurosci Abstr 17:630
Vaughan HG Jr, Arezzo JC (1988) The neural basis of event related potentials. In: Picton TW (ed) Human event-related potentials. (EEG handbook, vol 3) Elsevier, Amsterdam, pp 45–87